Title

Dynamic Bubbling Balanced Proactive CO2 Capture and Reduction on a Triple-Phase Interface Nanoporous Electrocatalyst

Journal

Journal of the American Chemical Society, 146(31)

ISSN

0002-7863

Authors

Zhang, Wei

Yu, Ao

Mao, Haiyan

et al.

Publication Date

2024-08-07

DOI

10.1021/jacs.4c02786

Peer reviewed

`

Dynamic bubbling balanced proactive CO_2 capture and reduction on triple-phase interface engineered electrocatalyst

Wei Zhang[1,2†], Haiyan Mao[3,4†], Guangxia Feng[5], Cheng Li[6,7], Guanzhi Wang[1,2], Jinfa Chang[1], David Halat[3], Zhao Li[1,2], Yaping Shi[5], David W. Fox[1,9], Ao Yu[1], John R. Martinez[9], Lei Zhai[1,9], Meng Gu[6], Xiaonan Shan[5], Jeffrey A. Reimer[3], Yi Cui[4]*, and Yang Yang[1,2,8,9,10]**

1. NanoScience Technology Center, University of Central Florida, Orlando, FL, 32826, USA.
2. Department of Materials Science and Engineering, University of Central Florida, Orlando, FL 32826, USA.
3. Department of Chemical and Biomolecular Engineering, University of California, Berkeley, Berkeley, CA 94720, USA.
4. Department of Materials Science and Engineering, Stanford University, Stanford, CA, 94305, USA.
5. Electrical and Computer Engineering Department, W306, Engineering Building 2, University of Houston, Houston, TX, 77204, USA.
6. Department of Materials Science and Engineering, Southern University of Science and Technology, Shenzhen 518055, China.
7. School of Physics and Astronomy, University of Birmingham, Birmingham, B15 2TT, UK.
8. Renewable Energy and Chemical Transformation Cluster, University of Central Florida, Orlando, FL, 32826, USA.
9. Department of Chemistry, University of Central Florida, Orlando, FL 32826, USA.
10. The Stephen W. Hawking Center for Microgravity Research and Education, University of Central Florida, Orlando, FL, 32826, USA.

† Wei Zhang and Haiyan Mao contributed equally to this work

*Correspondence and requests for materials should be addressed to Jeffrey A. Reimer (reimer@berkeley.edu) (J.A.R.); Yi Cui (yicui@stanford.edu) (Y.C.); Yang Yang (Yang.Yang@ucf.edu) (Y.Y)

Abstract

The formation and preservation of the active phase of the catalysts at the triple-phase interface during CO_2 capture and reduction is intensively essential in improving the conversion efficiency of CO_2 electroreduction towards value-added chemicals and fuels under operational conditions. However, designing such ideal catalysts that can mitigate the parasitic hydrogen generation and prevent the degradation of the active phase during the CO_2 reduction reaction (CO_2RR) remains a significant challenge. Herein, we developed an interface engineering strategy to build a new SnO_x catalyst by grouping different expertises. This catalyst features a hierarchically porous structure coated with an organic F-monolayer that modifies the triple-phase interface in aqueous electrolytes, substantially reducing competing hydrogen generation and enhancing CO_2RR selectivity. This rationally designed triple-phase interface overcomes the issue of limited CO_2 solubility in aqueous electrolytes via proactive CO_2 capture and reduction. Concurrently, we utilized pulsed square-wave potentials to dynamically recover the active phase for CO_2RR, aiming to regulating the production of C1 products such as formate and carbon monoxide (CO). This ensures profoundly enhanced CO_2RR selectivity and durability. More impressively, we achieved a mechanistic understanding of the dynamic bubbling balanced CO_2 capture and reduction processes under pulsed square-wave potentials via *in-situ* Raman spectroscopy, by observing the potential-dependent intensity of Raman vibrational modes of the active phase and CO_2RR intermediates. This work will inspire materials design strategies by leveraging triple-phase interface engineering for emerging electrochemical processes, moving toward electrification and decarbonization.

Keywords: CO_2 capture; CO_2 reduction; triple-phase interface; interface engineering; porous materials

Introduction

Promoting CO_2 electroreduction to value-added chemicals and fuels is critically important for achieving global electrification and decarbonization targets by 2050.[1-3] The electrocatalytic CO_2 reduction reaction (CO_2RR) converts CO_2 gas into carbon-containing chemicals such as C1 (carbon monoxide (CO), formic acid (HCOOH), methanol, methane, etc.), C2 (ethylene, ethanol, acetate, ethylene glycol, etc.), and C2+ products (propanol, propionaldehyde, etc.), depending on the specific reaction pathways on the catalysts.[4] Among the major products, C1 products (particularly HCOOH and CO) are considered the most economically viable due to their high energy storage capacity and broad applications as building blocks in the chemical manufacturing industry.[5] While promising, conventional catalysts for C1 products, such as Pd, Bi, and Cu, are either prohibitively expensive or exhibit low selectivity, making them unsuitable for scalable usage. Apart from the low selectivity of the catalysts, a major challenge is to devise an optimal solid-liquid-gas triple-phase interface that could enhance CO_2RR conversion efficiency by overcoming the limited CO_2 solubility (~0.034 M under ambient conditions) in aqueous electrolytes as well as flooding on the catalysts.[6,7] In addition, diminished CO_2RR activity over prolonged periods due to catalyst degradation and surface reconstruction greatly limits large-scale implemetation. Thus, dissecting the structure-property relationships and exerting dynamic control of the surface active phase will prove advantageous in improving the selectivity and durability of CO_2RR catalysts.

Tin oxides (SnO_x), being cost-effective, earth-abundant, and non-toxic materials, have recently been reported to have high selectivity towards HCOOH by a 2-electron transfer pathway in CO_2RR, attributed to the preferred intermediate of *OCHO formed due to its high oxygen affinity. Recent studies have focused on enlarging the active surface area of SnO_x by developing various nanostructures to facilitate mass and electron transfer for CO_2RR.[8-12] Nevertheless, a decrease in CO_2RR efficiency was observed when the oxide-based active phase was partially reduced to the metallic phase (i.e., surface reconstruction), leading to increased hydrogen generation, one of the most competing and unresolved challenges in CO_2RR[13-15] Like other oxide-based catalysts, SnO_x undergoes significant surface reconstruction and function degradation in response to applied cathodic potentials.[16] These undesired atomic rearrangements or/and altered chemical states result in unstable and deactivated CO_2RR performance.[17] Hence, these defeciencies motivates key studies to understand the chemical transformation at the triple-phase interface microenvironment when designing oxide-based catalysts aimed at suppressing hydrogen generation and augmenting the conversion efficiency of dissolved CO_2.[18,19]

Nature materials such as lotus, possessing unique micro-nano structures can greatly support water droplet and trap air in their nanostructures. Inspired by nature, to deliver high concentration of encapsulated CO_2 gas bubbles to the electrode surface when immersed in aqueous electrolytes, interface engineering strategies, particularly morphology control, have been employed to enhance the gasphilic property of the catalysts for improving CO_2 gas molecule mass transfer and maintaining alkaline reaction condition.[20,21] Moreover, microenvironments (e.g., CO_2 affinity, local electric field, exposure of active facets, etc.) at the triple-phase interface of the catalysts can also be optimized to favor CO_2RR.[22-24] However, the degradation of gasphilic behavior at the

triple-phase interface is often encountered due to surface reconstruction of the catalysts under operational conditions.

In this work, we designed a bio-inspired gasphilic SnO_x porous film electrode that mimics unique lotus surface structure to modulate the reaction microenvironment of gasphilicity, increasing local CO_2 concentration via a proactive CO_2-capturing process near the electrode surface. By grouping different expertises, this approachforms a favorable triple-phase interface for CO_2RR. We validated the concept that CO_2RR selectivity can be significantly improved by further modifying the triple-phase interface via a surface coating of a self-assembled organic F-monolayer (SAFM). Specifically, we probed the dynamically bubbling balanced triple-phase interface and monitored the surface chemical state changes of the electrode using *in-situ* Raman techniques under square-wave pulsed potentials, facilitating a deeper mechanistic understanding of the structure-property relationships relevant for CO_2RR. We also verified the crucial role of dynamic recovery of the active phase in maintaining stable CO_2RR, specifically targeting the production of desired C1 products, throughout long-term operation using pulsed potentials. The proposed interface engineering strategy concludes with a new horizon on regulating and preserving favorable microenvironments at the triple-phase interface for not only CO_2RR but also other electrochemical processes aimed at electrification and decarbonization.

Results

"Lotus" structured gasphilic porous film electrode

To mimic the unique lotus surface morphology and improve the gasphilc behavior of electrode during CO_2RR, we developed a series of SnO_x film electrodes with a hierarchically porous morphology using electrodeposition and anodization, followed by thermal annealing and surface

coating of SAFM (See **Methods** for detailed experimental procedures). The fabricated "Lotus" structured porous film electrode possessing unique micro-nano structures that shows incredible superhydrophobic behavior of which water can easily slides off the electrode (**Figure 1a**). We performed CO_2RR process in a H-type cell filled with CO_2-saturated aqueous electrolyte. More surprisingly, the porous film electrode shows "plastron"-like triple-phase interface in the aqueous electrolyte, which enables dynamic liquid CO_2 bubbling balanced capture and reduction process via combination of morphology control and surface chemistry (**Figure 1b**). Moreover, this unique porous film fabrication and configuration design significantly improved the CO_2RR selectivity towards CO and formate due to enhanced local CO_2 concentration thus mass transfer process at the triple-phase interface (**Figure 1c**). More details will be discussed in the following sections.

Thermal Modulation of Active Phase

Sn oxides (SnO_x) exhibit higher oxygen affinity and CO_2RR activity compared to metallic Sn due to their unique chemical structure, which stabilizes $*CO_2^{\bullet-}$. However, it remains elusive how the stoichiometry of Sn and O in SnO_x influences CO_2RR selectivity towards the production of CO and formate.[25,26] In general, different stoichiometry ratios in SnO_x leads to different material properties due to the contrasting intrinsic semiconductor characteristics of p-type SnO and n-type SnO_2, which can be tailored by thermally-induced phase transformation.[27,28] The as-prepared sample after anodization has been denoted $SnO_{1.82}$. Thermally annealing the anodized samples at 200 °C, 300 °C, and 450 °C yielded samples denoted as $SnO_{1.33}$, $SnO_{0.98}$, and $SnO_{1.57}$, respectively. Note that the stoichiometric ratios between Sn and O for all samples were determined by scanning transmission electron microscopy-energy-dispersive X-ray (STEM-

EDS) mapping. Our results indicate that the most effective SnO_x for CO_2RR comprises amorphous SnO and polycrystalline SnO_2 in $SnO_{0.98}$ (as discussed later in this article).

To reveal the unique micro-nano structure, the top-view scanning electron microscopy (SEM) image (**Figure 2a**) shows approximately 20 nm nanopores uniformly distributed on the film electrode (**Figure 2b**). A cross-sectional SEM image reveals a 4 μm-thick SnO_x porous layer grown on Cu foil (**Figure S1**). This unique hierarchically porous structure enables gas trapping due to well-establised micro-nano structures for enhanced gasphilicity, aiding in the creation of an engineered triple-phase interface for CO_2RR. Transmission electron microscopy (TEM) was utilized to reveal the phase composition of SnO_x porous films annealed at different temperatures. The surface layers of the samples were analyzed instead of the bulk to prevent the potential damage to the porous framework by the energetic e-beam used in TEM. Therefore, all the crystal lattice and phase information presented below pertains to the top porous layer of the film. During thermal treatment, the surface of the porous film undergoes phase transformation. The original $SnO_{1.82}$ was found to have a polycrystalline SnO_2 structure, as indicated by the diffraction pattern and a stoichiometric ratio of 1.82 between O and Sn detected by energy-dispersive X-ray (EDX) elemental analysis. This suggests that the surface layer of the anodized sample consists of the crystallized SnO_2 phase and an amorphous SnO phase (**Figure 2c and Figure S2**). Upon annealing at 200 ºC, $SnO_{1.82}$ was found to transform into $SnO_{1.33}$, showing the formation of a new polycrystalline SnO phase alongside the SnO_2 phase and amorphous SnO phase. This transformation is confirmed by high-angle annular dark-field imaging-scanning transmission electron microscopy (HAADF-STEM) images and the diffraction patterns labelled for the (110), (012), (10$\acute{2}$), and (101), (200), (10$\acute{1}$) planes for SnO and SnO_2, respectively (**Figure 2d and**

Figure S3). The newly formed crystalline SnO phase is likely crystallized from the amorphous phase by thermal annealing. Moreover, $SnO_{1.33}$ was further transformed into $SnO_{0.98}$ by increasing the annealing temperature to 300 ºC. Note that the decreased oxygen content from 1.83 to 0.98 was attributed to the thermal-driven migration of surface oxygen to the bottom bulk part of the film.[29,30] $SnO_{0.98}$ exhibits an oxygen-deficient phase composition consisting of the amorphous phase and polycrystalline SnO_2, as determined from the diffraction pattern of (101), (211), and (110) planes of SnO_2 (**Figure 2e**). Moreover, the local interplanar spacing of 0.214 nm was assigned to SnO_2 (210), and the stoichiometry was unraveled by EDX elemental analysis (**Figure S4**).[31] Upon further annealing of the porous film at 450°C, $SnO_{1.57}$ displays the coexistence of the amorphous SnO phase and crystalline SnO_2 (**Figure 2g**), as identified by HAADF images and EDX elemental analysis (**Figure S5**). The deliberate thermal-driven phase transformation allows for modulation of the oxygen-deficient $SnO_{0.98}$ phase to obtain a modified triple-phase interface for efficient CO_2RR, which will be discussed later.

X-ray diffraction (XRD) was also conducted to further examine the bulk structures of all the porous films (**Figure S6**). Broad diffraction peaks of amorphous SnO_x (2θ = 20-40°) were identified in $SnO_{1.82}$, $SnO_{1.33}$, and $SnO_{0.98}$, indicating gradual phase transformations driven by thermal treatment at different temperatures. Prior to annealing, except for strong diffraction peaks from the substrate (Cu and Sn), $SnO_{1.82}$ does not exhibit any clear peaks. Conversely, $SnO_{1.33}$ shows a SnO (112) peak located at 50.7° (JCPDS No. 6-395), indicating the formation of a new phase after annealing. Compared with $SnO_{1.33}$, $SnO_{0.98}$ displays additional SnO phases indicated by (101) and (002) diffractions at 29.8° and 37.1°, respectively, suggesting more crystalline SnO bulk phases formed at 300 °C. However, at a higher annealing temperature of 450 °C, the phase

transformations culminate in the appearance of three broad peaks at 26.6°, 33.8°, and 51.7°, corresponding to SnO_2 (110), (101), and (211), respectively (JCPDS No. 41-1445). Other labeled Sn and Cu XRD peaks in the samples derive from the electrodeposited Sn and substrate.

To further unravel the intrinsic structure of the samples, Raman spectroscopy was used to probe the vibration mode of the lattice structure (**Figure 2g**). $SnO_{1.82}$ predominantly exhibits a broad vibrational peak centered at 514 cm^{-1}, suggesting a majority amorphous phase, with other vibrational peaks being less pronounced. $SnO_{1.33}$ features two broad but less intense peaks around 100 cm^{-1} and 210 cm^{-1}, which correspond to E_g and A_{1g} modes of the crystalline SnO phases, but a broad peak centered at 544 cm^{-1} indicates the amorphous phase remains dominant.[32] By contrast, $SnO_{0.98}$ displays sharper and more intense E_g and A_{1g} peaks compared to $SnO_{1.33}$, indicating the formation of the SnO crystalline phase. The broad peak spanning 482 cm^{-1} (E_g), 544 cm^{-1} (B_{1u}), and 623 cm^{-1} (A_{1g}) represents the transformation of lattice vibrations. However, more intense and sharper peaks located at 110 cm^{-1} (E_g), 210 cm^{-1} (A_{1g}), 659 cm^{-1} (E_u), 696 cm^{-1} (A_{2u}), and 752 (B_{2g}) cm^{-1}, were found in $SnO_{1.57}$, indicating a transformations from an amorphous structure to a more crystalline phase.[33] The Raman spectra areconsistant with the XRD results in revealing the bulk phase transformation in the samples, suggesting the successive phase transformation as the annealing temperatures increase.

X-ray photoelectron spectroscopy (XPS) was utilized to identify the chemical states of the porous films. The XPS Sn 3d spectrum (**Figure 2h**) of $SnO_{0.98}$ shows $3d_{5/2}$ and $3d_{3/2}$ peaks at binding energies (BE) of 487.1 eV and 495.6 eV, respectively. These values can be assigned to non-stoichiometric tin oxides (SnO_x), implying a mixture of chemical states in the sample, a finding that aligns with XRD and Raman results.[34] The XPS O 1s spectrum (**Figure S7a**) shows

binding energies of 530.7 eV and 532.2 eV that can be assigned to lattice oxygen and adsorbed hydroxy groups, respectively.[35] After surface functionalization with a self-assembled F-contained monolayer (SAFM), XPS survey spectra of $SnO_{0.98}$-F display the presence of F as compared with $SnO_{0.98}$ (**Figure S8**), indicating successful linkage of SAFM to the sample via Si-O bonds, as confirmed by deconvolution of XPS Si 2p and F 1s spectra at BE of 103 eV and 688.5 eV, respectively (**Figure S7b,c**). Moreover, the detection of -CF_3 (294.4 eV) and -CF_2 (291.8 eV) functional groups from XPS C 1s spectra (**Figure S7d**) further confirms the existence of SAFM, which plays a key role in interface engineering of the sample, contributing to the mechanism of repulsive interaction between water and F-containing molecules during CO_2RR.[36] In addition, the CO_2 molecules exhibit physisorption on the porous film, suggesting enhanced CO_2 capture capacity within the porous structure of the film, as evidenced by the direct ^{13}C NMR spectrum of $^{13}CO_2$-dosed $SnO_{0.98}$-F which shows a significant resonance around 123.0 ppm (**Figure 2i**).

Enhanced CO_2 Capture at "Plastron"-Like Triple-Phase Interface

Biomaterials found in organisms such as insects and spiders facilitate underwater breathing. These creatures can survive when submerged in water because of their rough and hairy skin that can trap dissolved oxygen in the "plastron" layer.[37-39] Drawing inspiration from these natural features, we employed interface engineering through morphology control and self-assembly coating to construct an artificial "plastron"-like interface (**Figure S9**). This design enables gas-breathing capabilities and increases the local CO_2 concentration near the electrode surface of $SnO_{0.98}$-F. Note that the term "bio-inspired gasphilic porous film" (BGPF) is used in the following discussion to represent the "plastron"-like interface of $SnO_{0.98}$-F. Moreover, all other non-SAFM coated control samples were referred to as non-BGPF for easy comparison. Confocal

laser scanning microscopy (**Figure 3a**) shows the "trough-ridge" surface topology of the BGPF electrode, indicative of a rough surface morphology with a surface roughness of 0.91 ± 0.12 μm and max height of 6.23 ± 0.9 μm (**Figure S10**). These micro-structural characteristics are the result of our proposed electrochemical synthesis for mimicked structure. Moreover, besides the phase modulation, another advantage of the thermal treatment is the removal of the surface hydrophilic groups that remained within the porous structure of BGPF after electrochemical synthesis. Evidence for the thermal removal of the surface hydrophilic group came from the reduced amount of hydroxyl group on BGPF (31%) compared with non-BGPF (41%), as shown by the O 1s XPS spectra (**Figure S11**) and contact angle measurements (**Figure S12**). As a result, the BGPF shows superior hydrophobic properties with a contact angle of 158° compared to non-BGPF (**Figure S12**), owing to the water-repellent behavior conferred by the combination of the unique hierarchically porous morphology and the SAFM surface coating.[40] In addition, sliding behavior experiments in **Video S1a,b** show that water droplets can easily slide off the BGPF electrode, demonstrating the water-repellent and gasphilic features of the electrode.

To visually probe the electrode-electrolyte interactions at the triple-phase interface of the porous films, we utilized an underwater camera to record the solid-liquid-gas interface near the electrode during CO_2RR in a CO_2-saturated electrolyte. We compared the surface state of the gasphilic BGPF with that of the superhydrophilic non-BGPF electrode. **Figure S13a** reveals gas bubbles confined in the porous structure of the BGPF electrode, a result of the "plastron" effect. However, the non-BGPF electrode shows no signs of gas bubble affinity (**Figure S13b**), thereby verifying the gasphilic nature of the BGPF electrode that aids in gas capture and enhances the local CO_2 concentration. Moreover, the unique surface morphology of the BGPF

electrodecombined with the SAFM coating on the porous film, allows for self-capturing CO_2 capabilities in a CO_2-saturated 0.5 M $KHCO_3$ electrolyte. In particular, we captured videos displaying the dynamic states of surface bubbling on the BGPF electrode under various constant potentials underwater, and analyzed the bubble nucleation and growth processes. **Figure 3b** illustrates the changes in the surface morphological images during CO_2 capture under different applied potentials. There is a noticeable increase in dynamic bubbling from 0 V to -0.4 V. We also calculated and compared the estimated capture sites and volumes of CO_2 bubbles captured at various potentials per unit area (**Figure S14**). Following a cyclic voltammetry (CV) scan intended to clean and activate the electrode, different constant potential windows were scanned (0 V, -0.2 V, -0.4 V, -0.6 V, and -0.8 V). The corresponding numbers of bubble capture sites were obtained, validating the potential-dependent nature of the bubble capturing and nucleation processes (**Figure S15**). As shown in **Figure 3c**, the bubble-capturing process peaks at around -0.4 V and begins to decrease as the potential becomes more negative, implying instant consumption of some captured CO_2 molecules by CO_2RR. Remarkably, the dynamic process of CO_2 nucleation and bubbling was revealed in **Video S3**, showcasing the CO_2 self-capturing process on the BGPF electrode following a CV scan conducted under various potentials. Variations in the dynamic CO_2 bubbling rates was observed in the series of videos following frame subtraction, confirming the CO_2 self-capture process. This process is facilitated by an optimized triple-phase interface that significantly enhances the local CO_2 concentration and optimizes the microenvironment required for CO_2RR. In contrast, the superhydrophilic non-BGPF electrode shows a negligible change in surface bubbling states (**Video S4**), emphasizing the importance of surface coating in our proposed interface engineering. The effective CO_2

capturing process, as described above, critically influenced the local microenvironment near the electrode surface. This insight not only sheds light on novel electrode designs for efficient triple-phase interface engineering, but also provides a solution to the challenge of limited CO_2 solubility when carrying out CO_2RR in aqueous solutions.

To gain mechanistic understanding of the impact of gasphilicity, enabled through interface engineering, on the local microenvironment for CO_2RR, we examined the relationship between the electrochemically active surface area (ECSA) and the gasphilicity of the samples, confirming the critical role of our proposed interface engineering in tuning the local microenvironment.[41,42] **Figure 3d** shows the electrochemical double-layer capacitance of the porous films, calculated from CV tests (**Figure S16**). This measure correlates proportionally with the ECSA, which reflects the surface area wetted by the electrolyte. Among all samples, the BGPF electrode demonstrates the lowest capacitance of 0.25 mF/cm^2, owing to the "plastron" effect at the engineered triple-phase interface. An efficient triple-phase interface has a relatively low ECSA because gas bubbles encapsulated at the surface prevent the electrolyte from inundating the electrode. Thus, the well-established triple-phase interface of BGPF suggests a significantly improved local CO_2 concentration and microenvironment that may promote CO_2RR. In contrast, non-BGPF $SnO_{1.82}$ shows the highest capacitance of 3.27 mF/cm^2 among the samples, due to increased contact between the electrode and electrolyte, possibly resulting in heightened competition between the hydrogen evolution reaction (HER) and CO_2RR. The non-BGPFs $SnO_{1.33}$, $SnO_{0.98}$, and $SnO_{1.57}$ display intermediate capacitances of 2.67 mF/cm^2, 1.26 mF/cm^2, and 1.31 mF/cm^2, respectively. These measurements reflect varying interface properties induced by

phase modulation, confirming that the unique gasphilic morphology and surface coating of the samples improves the microenvironment at the triple-phase interface.

To further understand how the gasphilic feature of the BGPF electrode affects the microenvironment at the triple-phase interface, where CO_2 gas has a strong affinity to the solid electrode, we performed an analogous study of the oxygen evolution reaction (OER) process, comparing the gas-evolving properties of a sample with a hierarchically porous surface and one with a flat surface. As shown in **Figure S17**, we compared linear sweep voltammetry (LSV) and chronopotentiometry curves for OER on the BGPF electrode, non-BGPF electrode, and flat SnO_x electrode. The BGPF electrode shows a significantly lowest current density of 12.0 mA/cm^2 at a potential of 2.0 V in the LSV curve, compared to the non-BGPF electrode (50.7 mA/cm^2 at 2.0 V) and flat SnO_x electrode (60.4 mA/cm^2 at 2.0 V). This result suggests that the captured gas in the BGPF electrode limits the contact area between the electrode and electrolyte. Furthermore, the BGPF electrode exhibits an unstable and fluctuating i-t curve at a constant current density of 5 mA/cm^2 caused by the accumulation of generated gas bubbles on the surface of the BGPF electrode, providing additional evidence of enhanced gas capture capability of the electrode and an increased affinity of the gas bubbles to the electrode.[43]

Improved CO_2RR at Modified Triple-Phase Interface

Efficient CO_2RR demands a modified triple-phase interface that can be achieved through interface engineering and the rational design of the electrode structure. These aspects play a central role in regulating the gasphilic microenvironment for the reactions.[44] Herein, we demonstrate the effectiveness of the rationally designed BGPF, which has a modified triple-phase interface, for CO_2RR conversion to C1 products (e.g., CO and formate). **Figure 4a** schematically

depicts the function and CO_2RR reaction mechanism of the BGPF electrode. The synergistic combination of unique surface morphology control with the SAFM surface coating facilitates the formation of an artificial "plastron"-like interface. Additionally, the modified triple-phase interface can efficiently and proactively capture and subsequently reduce CO_2 in a CO_2-saturated aqueous medium, due to its gasphilic characteristics that are known collectively as the Cassie state.[45] This process suppresses the parasitic generation of hydrogen by repulsion of water molecules from the electrode surface, thus improving the conversion efficiency of CO_2RR against HER.[40] The schematically depicted CO_2RR process is explicitly observed in **Video S2**, in which the saturated CO_2 molecules dissolved in the electrolyte are self-captured by the electrode, followed by nucleation, growth, and bubbling.

The electrocatalytic CO_2RR performance of the samples was evaluated in an H-type cell filled with the CO_2-saturated 0.5 M $KHCO_3$ electrolyte. All voltages mentioned below are referred to the reversible hydrogen electrode (RHE). Cyclic voltammetry (CV) was utilized to record the oxidation and reduction peaks of the samples, revealing two broad anodic and cathodic peaks in the CO_2-saturated electrolyte. Conversely, in the N_2-saturated electrolyte solution, two sets of clear anodic and cathodic peaks were observed at 0.15 V and -0.25 V. These peaks correspond to the oxidation of Sn^0 to $Sn^{2+/4+}$ and reduction of $Sn^{2+/4+}$ to Sn^0, respectively (**Figure S18**), suggesting the presence of a mixed phase in $SnO_{0.98}$. Chronoamperometry (**Figure S19**) was conducted to study the faradaic efficiency (FE) and current density of CO_2RR under different potentials. The gaseous and liquid products were analyzed through gas chromatography (GC, **Figure S20**) and ^{1}H nuclear magnetic resonance (NMR, **Figure S21**), respectively. After coating SAFM on the surface of the samples, the BGPF electrode demonstrates CO_2RR with a

partial current density of 5.7 mA/cm^2 at -1.1 V, a performance that exceeds all other control samples in this work (**Figure 22a**). To unravel the impact of SAFM coating on the electrode surface, we also investigated CO_2RR in samples without SAFM coating. The same trend was observed for the non-BGPF electrodes with CO_2RR partial current densities of 4.3 mA/cm^2, 2.9 mA/cm^2, 3.7 mA/cm^2, and 4.1 mA/cm^2 for $SnO_{0.98}$, $SnO_{1.82}$, $SnO_{1.33}$, and $SnO_{1.57}$, respectively (**Figure S22b**). However, the SAFM-coated samples exhibit higher CO_2RR partial current densities than their counterparts without the SAFM coating, implying that the coating further modifies the microenvironment, reducing the non-CO_2RR faradaic current.

Moreover, we also compared the CO_2RR selectivity of BGPF and other control electrodes (e.g., $SnO_{1.82}$-F, $SnO_{1.33}$-F, and $SnO_{1.57}$-F) at constant potentials of -0.7 V, -0.9 V, and -1.1 V, as shown in **Figure 4b.** The BGPF electrode shows an CO production faradaic efficiency of 26.3%, 14.3%, and 6.7%, accompanied by a formate production faradaic efficiency of 55.1%, 68.2%, and 77.5% at -0.7 V, -0.9 V, and -1.1 V, respectively, surpassing all other SAFM-coated control samples. Note that the $SnO_{1.57}$-F sample shows much lower faradaic efficiencies for CO and formate (8.5%, 9.7%, and 5.1% for CO and 10.1%, 58%, and 63% for formate at -0.7 V, -0.9 V, and -1.1 V, respectively), implying suboptimal CO_2RR performance due to unsuitable mixed phase present in the sample even with SAFM coating. This observation underscores the significance of thermal-driven phase modulation in improving CO_2RR selectivity.

In order to validate the significance of the unique porous morphology endowed by our proposed interface engineering, we conducted tests on the flat SnO_x film electrode (**Figure S23**). The drastic decrease in total CO_2RR efficiencies (less than 50%) across all potentials suggests that parasitic HER tends to overshadow the CO_2RR electrochemical processes. This result

highlights the key role of morphology control for the suppression of HER. We also observed that all SAFM-coated samples demonstrate better CO_2RR selectivity than their uncoated counterparts (**Figure S24**), reaffirming the importance of SAFM in enhancing the CO_2RR selectivity due to further enhancement of gasphilicity at the triple-phase interface.[46] Among these samples, BGPF shows the highest CO_2RR faradaic efficiency of 84.2% with a partial current density of 5.7 mA/cm^2 at -1.1 V. This further confirms that the synergistic combination of morphology control and surface coating can improve the CO_2RR performance at the modified triple-phase interface, as proposed in our interface engineering design.[47]

We also conducted a comprehensive comparison of the HER faradaic efficiency in order to relate the surface properties of the porous films and the CO_2RR performance (**Figure 4c**). The non-BGPF $SnO_{0.98}$, without a coating layer, shows a lower HER efficiency (10.9-18.7% at -0.7 to -1.1 V) compared to other non-BGPF control samples (e.g., $SnO_{1.82}$, $SnO_{1.33}$, and $SnO_{1.57}$). This implies that the presence of the mixed phase of $SnO_{0.98}$ leads to the lowest selectivity towards H_2 production, thereby contributing to a higher partial current density for CO_2RR. Moreover, the measured contact angle (152.2°) of $SnO_{0.98}$, which is considerably higher than that of the other non-BGPF control samples, illustrates its superior gasphilicity arising from superhydrophilicity. This characteristic is attributed to its unique porous morphology and the presence of mixed chemical states attained by our proposed interface engineering process. As expected, all SAFM-coated porous films show remarkably reduced hydrogen production compared to their uncoated counterparts. In particular, BGPF displays further enhanced gasphilicity (contact angle of 158°), and surprisingly the lowest HER efficiency (7.5-9.8% at -0.7 to -1.1 V), compared to all other control samples. The ability to suppress hydrogen generation while increasing CO_2RR faradaic

efficiency, facilitated by the modified triple-phase interface.This underscores the critical role of our proposed interface engineering in optimizing CO_2RR performance.

Linear sweep voltammetry (LSV) was also utilized to discern the CO_2RR selectivity of the samples in the N_2- and CO_2-saturated 0.5 M $KHCO_3$ electrolytes. Within a potential window of -0.7 to -1.1 V, both SAFM-coated and uncoated samples demonstrate higher cathodic current density in the CO_2-saturated electrolytes compared to the N_2-saturated electrolytes, confirming their electrocatalytic activity for CO_2RR. However, the LSV current densities of all SAFM-coated samples (e.g., BGPF, $SnO_{1.33}$-F, $SnO_{0.98}$-F, and $SnO_{1.57}$-F) in the CO_2-saturated electrolytes are lower than the uncoated ones, suggesting a reduction in the current density associated with HER due to the repulsion of protons from the electrode surface (**Figure S25a,b**). The LSV curves measured in the N_2-saturated electrolytes indicated that BGPF exhibits the lowest current density related to hydrogen generation, which aligns well with the previously determined HER faradaic efficiency. Moreover, other SAFM-coated samples (e.g., $SnO_{1.82}$-F, $SnO_{1.33}$-F, and $SnO_{1.57}$-F) display less hydrogen generation compared to their uncoated counterparts, further validating the improvement of gasphilicity through surface coating (**Figure S25c,d**). In summary, based on all the aforementioned discussions, we have demonstrated that a balance of active phase modulation, morphology control, and surface coating is pivotal for optimizing the triple-phase interface when designing new catalysts for CO_2RR and other applications.[39,48]

Mechanistic Understanding of Dynamic Recovery in Active Phase

SnO_x catalysts in particular may undergo surface reconstruction towards metallic tin, a process facilitated by the facile failure of Sn-O bonding during CO_2RR. This significantly lowers the corresponding faradaic efficiency of CO_2 electrolysis and leads to the undesired hydrogen

generation.[49-51] In contrast to applying constant potentials to the electrode, pulsed electrochemistry using a square-wave potential, composed of specific anodic and cathodic potentials, can dynamically steer reaction products and suppress hydrogen generation for CO_2RR. The applied anodic potential alters the surface properties of the electrode, including morphology, chemical state, and surface adsorbates, thereby tuning the reaction selectivity.[52-54] To dynamically recover the active phase and further tune the microenvironment for stable CO_2RR, we cyclically applied a square wave potential to BGPF at different cathodic potentials for Δt_c = 30s and then at an anodic potential of 0.2 V for Δt_a = 5s (**Figure S26**). As shown in **Figure 4d**, hydrogen production was exceptionally lower by nearly 4% across all applied potentials from -0.7 V to -1.1 V, compared to results obtained under constant potentials. This highlights the beneficial role of pulsed potentials in enhancing possible electroabsorption of hydroxides on the electrode surface at applied anodic potentials. Compared to the CO_2RR performance obtained under constant potentials applied to BGPF, we observed similar CO production, but formate production increased by about 5% in the sample tested with pulsed potentials. This indicates that the applied anodic potentials facilitate the dynamic recovery of the active phase and the regulation of the local microenvironment. Moreover, an electrochemical stability test using cyclically pulsed potentials (Δt_a = 5s at 0.2 V and Δt_c = 30s at -0.8 V) was performed for 10 h. Strikingly, the formate production faradaic efficiency (~68 %) was well maintained under pulsed potentials (**Figure 4e**), whereas that of formate declined to 56%, accompanied by an increase in hydrogen generation (~5% to 13%, **Figure S27**) when tested under a constant potential of -0.8 V. Moreover, a more than 10% increase in the current density retention was obtained when switching from constant to pulsed potential mode (**Figure S28**).The unaltered porous

morphology and well-maintained hydrophobic surface were confirmed by SEM (**Figure S29**) and contact angle measurements (**Figure S30**), respectively. Additionally, the presence of the F signal (688.4 eV) after electrochemical tests as detected by XPS (**Figure S31**) doubly confirms the robust adherence of the coating layer to the sample surface.

To gain a mechanistic understanding of the function of the pulsed square wave-potentials, particularly the anodic potentials, in tuning the active phase of the sample to enhance the selectivity of CO_2RR, an *in-situ* Raman technique was used. This allowed us to probe the variations of the vibrational mode under electrochemical conditions. We applied both constant (0.2 V and -0.8 V) and cyclically pulsed potentials (Δt_a = 5s at 0.2 V and Δt_c = 30s at -0.8 V) separately on BGPF and non-BGPF samples of $SnO_{1.82}$. As shown in **Figure 5a**, upon application of a constant oxidative potential at 0.2 V for 60 s, we observed a sharp increase in intensity in both E_g (476 cm^{-1}) and A_{1g} (623 cm^{-1}) vibrational modes in BGPF, compared to the sample with no bias applied, suggesting the oxidative potential could induce surface lattice vibration that might be responsible for tuning selective CO_2RR towards desired C1 products.[55] In these two Raman active modes, the oxygen atoms vibrate in a specific direction while Sn atoms remain stationary. This implies a dynamic oxidative potential can replenish the surface oxygen, potentially maintaining a high oxygen affinity for *OCHO.[15] We also noticed a rise in the above-mentioned peak intensities under pulsed conditions (illustrated by light blue and brown curves in **Figure 5a**) for BGPF. These peaks are higher than those observed at the constant potential of -0.8 V (green solid curves in **Figure 5a**), providing evidence for the superiority of a dynamic potential over a constant potential in recovering the performance of the active phase. **Figure 5b** outlines the changes in the Raman peak intensity of E_g and A_{1g} modes under constant potential

and pulsed potentials applied to both BGPF and non-BGPF samples. Both E_g and A_{1g} intensities increase upon application of oxidative potentials for BGPF. Furthermore, these intensities are higher for pulsed working conditions compared to constant potential operation, as highlighted in the shaded area. In contrast, the characteristic peaks for non-BGPF exhibit steady peak intensities across all conditions, indicating no surface-sensitive perturbation of E_g and A_{1g} under oxidative conditions. Conversely, under a constant reductive condition of -0.8 V for 60s, both BGPF and non-BGPF samples exhibit decreased surface vibrational mode intensity compared to the initial state. This suggests a continuous degradation of the active phase under solely reductive conditions (**Figure S32**). Moreover, the increased vibrational peak intensity observed for BGPF aligns well with the enhanced formate production faradaic efficiency under pulsed conditions. This increase is related to the peak intensity of the A_{1g} (623 cm^{-1}) mode, as established by previous work.[50]

We further explored the activation of CO_2 and the adsorption of the $*CO_2^{\bullet-}$ intermediate on the electrode using *in-situ* Raman spectroscopy (**Figure S33**). This analysis revealed changes in the intensity and vibrational frequency of Raman-active intermediates as the potentials were scanned. This is attributed to the electrochemical Stark effect, which relates to the orientation of the adsorbates under an electric field. $*CO_2^{\bullet-}$ is believed to be the first intermediate when CO_2RR proceeds towards C1 products such as formate and CO, thus playing an important role in promoting CO_2RR kinetics.[56] We plotted the effect of electrochemical potentials on intensity and Raman shifts of asymmetric ($\upsilon_{as}CO_2^{-1}$, ~1600 cm^{-1}) and symmetric ($\upsilon_sCO_2^{-1}$, ~1335 cm^{-1}) stretching modes of $*CO_2^{\bullet-}$ in **Figure 5c,d,** which are in line with the previous study.[57] Our results show that both intensities of $\upsilon_{as}CO_2^{-1}$ and $\upsilon_sCO_2^{-1}$ are highest at 0.2 V and decrease as the

potential is scanned negatively to the representative working potential of -0.8 V for BGPF (blue square labeled dash curve in **Figure 5c**,**d**), indicating the consumption of $*CO_2^{\bullet-}$ on the electrode under reductive conditions. Moreover, the $\upsilon_{as}CO_2^{-1}$ peak undergoes a redshift from 0.2 V to -0.8 V, attributed to the Stark shift effect due to variations in local electric fields (black square labeled dashed curve in **Figure 5c**), reflecting the potential-dependent chemisorbed state of the intermediate. Moreover, under pulsed conditions the intensity of $*CO_2^{\bullet-}$ remains higher than under the constant potential (shown in the shaded area), which can be attributed to dynamic recovery of the active phase of the catalyst.[57,58] In contrast, non-BGPF samples did not display obvious changes in intensity or frequency under any conditions (blue asterisk labeled dashed curve in **Figure 5c** and black asterisk labeled dashed curve in **Figure 5d**), further confirming the significance of maintaining an appropriate phase composition for enhancing CO_2RR activity and long-term stability.

Conclusion

In summary, we rationally designed a bio-inspired, gasphilic SnO_x porous film electrode to regulate the microenvironment at the triple-phase interface. Through thermal annealing, we established an optimized mixed phase of amorphous SnO and polycrystalline SnO_2 within the porous film, which facilitates the selective conversion of CO_2 to economically advantageous C1 products such as formate and CO. Additionally, a SAFM coating was applied to the porous film to further modify the local microenvironment at the triple-phase interface, resulting in an unconventional "plastron"-like layer underwater. This rationally designed porous film demonstrated the ability to self-capture CO_2 at the modified triple-phase interface in the CO_2-saturated electrolyte. This approach increases the local CO_2 concentration, overcoming the issue

of limited CO_2 solubility that typically plagues conventional CO_2RR conducted in aqueous electrolytes. Furthermore, we adopted a technique that employs pulsed square-wave potentials to direct the CO_2RR conversion toward the preferred formate product and ensure long-term stable CO_2RR activity term. With *in-situ* Raman spectroscopy, we identified clear potential-dependent shifts and variations in intensity for vibrational modes of E_g and A_{1g} in $SnO_{0.98}$-F and the first $CO_2^{\bullet-}$ intermediate, underscoring the critical role of dynamic recovery of the active phase in maintaining stable CO_2RR. As a result, we achieved a stable CO_2RR faradaic efficiency of ~85% throughout a 10-hour duration test in pulsed conditions. Our study validates the synergistic application of interface engineering for controlling the critical triple-phase interface for CO_2RR and beyond, providing indispensable insights for the efficient design of catalysts for emerging electrochemical processes aimed at electrification and decarbonization.

Methods

Chemicals. Tin (II) sulfate ($SnSO_4$, 98%, thermal scientific chemicals), Polyethylene glycol 4000 (PEG, thermal scientific chemicals), Potassium pyrophosphate ($K_4P_2O_7$, 95%, thermal scientific chemicals), Tridecafluoro-1,1,2,2-tetrahydro octyl)Trichlorosilane (Gelest), Oxalic acid dihydrate (HO_2CCO_2H, 98%, Alfa Aesar) were used as received. Deionized water (DI water, 18.2 MΩ·cm) was used to prepare all aqueous solutions. All analytical-grade chemicals were purchased without further purification.

Synthesis of $SnO_{1.82}$-(F), $SnO_{1.33}$-(F), $SnO_{0.98}$-(F), and $SnO_{1.57}$-(F) porous film electrodes. The facile electrodeposition (bottom-up) strategy was used to prepare the Sn film. All electrolytes were prepared with DI water (18.2 MΩ·cm), which was boiled and cooled down to room temperature to eliminate the dissolved oxygen. First, an electroplating solution was prepared by

dissolving 2.18 g $K_4P_2O_7$, 0.1415 g PEG, and 0.3533 g $SnSO_4$ into a 100 mL beaker and thoroughly stirring for 30 minutes. Then, the prepared solution was transferred into a homemade electrodeposition cell. In this setup, the copper foil served as the working electrode and platinum (Pt) mesh as the counter electrode. The resulting Sn metal layer on the Cu substrate (2 x 2.5 cm^2) was electroplated at a constant voltage of 2.9 V for 1 hour. The subsequent anodization was conducted at 9 V for 10 mins with Sn metal film as the working electrode and Pt mesh as the counter electrode in an electrolyte consisting of 0.05 M oxalic acid, producing $SnO_{1.82}$. The other catalysts, $SnO_{1.33}$, $SnO_{0.98}$, and $SnO_{1.57}$, were prepared via thermal annealing in air for 1 hour at 200 °C, 300 °C, and 450 °C, respectively. Finally, tridecafluoro-1,1,2,2-tetrahydrooctyl)trichlorosilane was used as an organic F-silane source to assemble a monolayer on the porous film surface using the vapor phase deposition method. Briefly, 1 μL of tridecafluoro-1,1,2,2-tetrahydrooctyl)trichlorosilane and the porous films were placed on two separate glass slides in a vacuum desiccator, and the pressure was reduced to 20 inHg for 30 minutes to obtain $SnO_{1.82}$-F, $SnO_{1.33}$-F, $SnO_{0.98}$-F, and $SnO_{1.57}$-F.

Materials Characterizations. The structure and morphology of the materials were characterized using a scanning electron microscope (SEM, ZEISS ultra-55), and a Keyence laser confocal microscope (VK X-3000). High-angle annular dark-field scanning transmission electron microscopy (HAADF-STEM) and energy dispersive (EDS) mapping were carried out using an FEI-Titan Cubed Themis G2 300 equipped with a probe aberration corrector. The crystal structure was analyzed by X-ray diffraction (XRD, Panalytical X'celerator multi-element detector with Cu Kα radiation source, λ = 1.54056 Å). The chemical state information was investigated by X-ray photoelectron spectroscopy (XPS Escalab 250Xi), calibrated with

reference to the adventitious C 1s, C-C peak at a binding energy of 284.6 eV. Raman spectroscopy (Horiba LabRAM confocal Raman microscope) employing a 532 nm green laser was used to probe the materials, where the calibrated Si wafer Raman band was around 520 cm^{-1}. ^{1}H nuclear magnetic resonance (NMR) spectra were collected on a Bruker AVANCE-III 400 MHz spectrometer, and NMR data were processed using the MestRenova package (v. 12.0.0). Solid-state NMR was performed at 500.12 MHz (for ^{1}H) on a Bruker Avance spectrometer using a Bruker narrow bore MAS probe.

***In-situ* Raman and surface morphology imaging measurement.** The home-built *in-situ* Raman microscopy module was coupled with an inverted optical microscope (Olympus IX83). A laser diode emitting a wavelength of 642 nm (Vortran Stradus) was collimated and focused on the electrode surface. The laser beam excited the Raman scattering signal from the sample after being directed at the surface through a dichroic mirror. To conduct in-situ Raman experiments in the electrolyte, a 20 X water immersion objective (working distance: 3.5 mm, N.A. 0.5, Thorlabs) was applied to focus the incident laser beam onto the sample and collect the scattered laser signals. During the *in-situ* Raman measurements, the scattered light collected by the objective was filtered through a long pass filter (670 nm, Chroma), directed into a Raman spectrometer (iHR550, Horiba) and recorded by a CCD (charge-coupled device) detector for further analysis. To monitor CO_2 capture and morphological changes of the sample during the experiments, a switchable bright-field imaging system was coupled to locate the sample surface and observe the morphological variations. A white light LED (Thorlabs) was directed to the system via a beam splitter and collimated onto the sample surface. A scientific CMOS camera

(Hamamatsu, C11440-42U30) was employed to record high-quality bright-filed images and videos of the sample surface, achieving a spatial resolution of ~300 nm.

Electrochemical Characterizations. All electrochemical measurements were carried out using an electrochemical workstation (WaveDriver 200, Pine research) in a standard three-electrode H-type cell separated by a Nafion membrane (117, fuel cell store) at room temperature. In this setup, the as-prepared porous films were clamped as the working electrode, a carbon rod functioned as the counter electrode, and Ag/AgCl (3 M) served as the reference electrode. The electrolyte used in this work for CO_2RR is 0.5 M $KHCO_3$ (pH = 7.4), which was saturated with CO_2 by bubbling gas for at least 30 minutes before each test. All potentials were calculated and referred to the reversible hydrogen electrode (RHE). All electrochemical experiments were recorded and analyzed by conducting cyclic voltammetry (CV), chronoamperometry (i-t), and linear sweep voltammetry (LSV). All LSV curves in this work were shown without iR compensation.

The overall electrochemical active surface area (*ECSA*) of porous films was estimated according to the double-layer capacitance. The CV experiments were conducted in the non-Faradic region at various scan rates from 10 mV/s to 100 mV/s. The double-layer charging or discharging currents were plotted associated with the scan rates, and the slope extracted from the curves offered the double-layer capacitance.

The evolved gas product collected from the H-type cell was analyzed using gas chromatography (GC-2014, Shimadzu) equipped with a thermal conductivity detector and a flame ionization detector. Each gas sample was promptly introduced into the instrument following a 15-minute stable run under chronoamperometry, with a flow rate maintained at 50

sccm. The faradaic efficiency of the gas products during CO_2RR was calculated based on the following equation:

$$FE_{CO2\,RR}=\frac{NFVn}{I_{total}}$$

where n is the number of electrons transferred during CO_2RR conversion, and N is 2 for both the H_2 and CO production. n is the mole amount of the products which can be calculated by the ideal gas equation ($n=\frac{pv}{RT}$), in which v is the gas product volume concentration measured from GC (**Figure S19**), p is the standard pressure of 101.325 kPa, R is the natural gas constant (8.314 J/mol·K), and T is the standard temperature of 298.15 K. F is the Faradaic constant, and V (ml/min) is the gas flow rate measured using a flow meter (Alicat Scientific). I_{total} is the total current in CO_2 electrolysis.

The partial current density of CO_2RR ($J_{CO2\,RR}$) is calculated via the equation below:

$$J_{CO2\,RR}=\frac{FE_{CO2\,RR}\cdot I_{total}}{electrode\ area}$$

The liquid product was quantified using nuclear magnetic resonance spectroscopy (NMR, Bruker, Avance 400). In brief, 500 μL catholyte after each experiment cycle was collected into a 20 mL vial, and 100 μL of D_2O and 100 μL of 7 mM Dimethyl sulfoxide (DMSO) were added and mixed uniformly. Then the 700 μL analyte was transferred into the NMR tube for quantification. ^1H NMR was conducted in water suppression mode. The concentration of formate was obtained by integrating the characteristic peak area and calculating based on the calibration curve (**Figure S20**).

Data availability

The authors declare that all data supporting the findings of this study are available within the paper and Supporting Information files.

Acknowledgements

This work was supported by National Science Foundation under Grant No. CMMI-1851674, CBET-1949840, and ACS PRF (65481-ND10). The XPS characterization was supported by the National Science Foundation NSF MRI: XPS: ECCS: 1726636, hosted in MCF-AMPAC facility, MSE, CECS, UCF. X.S. acknowledges the funding support from the USDA SBIR award (No. 2022-70012-36900 and 2019-33610-29769), University Training and Research for Fossil Energy Applications (DOE DE-FE-0032092), and the UL Research Institutes. The Raman characterization was supported by the National Science Foundation under Grant No. DMR 1920050 (MRI). The solid-state-NMR characterization was partly supported by the DOE, Office of Basic Energy Sciences, Division of Materials Sciences and Engineering (contract no. DE-AC02-76SF00515). J.A.R. acknowledges partial support from the ACT-PrISMa project, which has received joint funding from BEIS, NERC, and EPSRC (UK), funding from the Division of CCS R&D, DOE, and funding from the Office Fédéral de l'Energie (Switzerland). M.G. acknowledges the National Key Research and Development Project (2022YFA1503900), Shenzhen fundamental research funding (JCYJ20210324115809026, 20200925154115001, JCYJ20200109141216566), Shenzhen Science and Technology Program (Grant No. KQTD20190929173815000), Guangdong Innovative and Entrepreneurial Research Team Program (Grant No. 2019ZT08C044), and Guangdong scientific program (Contract no. 2019QN01L057). The TEM work (M.G.) was supported by the Pico Center at SUSTech CRF which receives support from the Presidential Fund and Development and Reform Commission of Shenzhen Municipality.

`

Conflict of interest

The authors declare no conflict of interest.

Author contributions

Y.Y., Y.C., and J.A.R led the project. W.Z. and H.M. designed and synthesized the materials and conducted the electrochemical measurements, SEM, XPS, XRD, and Raman characterizations. G.F., Y.S., and X.S. performed *in-situ* Raman characterization and microscope imaging and analyzed the data. C.L. and M.G. conducted the TEM characterization and analyzed the data. G.W., J.C., and Z.L. contributed to the electrochemical experiments and data discussion. D.W.F. and L.Z. performed water contact angle measurements. W.Z., A.Y., and J.M. contributed to the schematic diagram draft and discussion. All authors contributed to the data discussion and approved the manuscript.

References

1 Hepburn, C. *et al.* The technological and economic prospects for CO_2 utilization and removal. *Nature* **575**, 87-97 (2019).

2 Rogelj, J., Geden, O., Cowie, A. & Reisinger, A. Net-zero emissions targets are vague: three ways to fix. *Nature* **591**, 365-368 (2021).

3 Grim, R. G. *et al.* Transforming the carbon economy: challenges and opportunities in the convergence of low-cost electricity and reductive CO_2 utilization. *Energy Environ. Sci.* **13**, 472-494 (2020).

4 Pan, F. & Yang, Y. Designing CO_2 reduction electrode materials by morphology and interface engineering. *Energy Environ. Sci.* **13**, 2275-2309 (2020).

5 Li, Z. *et al.* Elucidation of the Synergistic Effect of Dopants and Vacancies on Promoted Selectivity for CO_2 Electroreduction to Formate. *Adv. Mater.* **33**, 2005113 (2021).

6 Kibria, M. G. *et al.* Electrochemical CO_2 Reduction into Chemical Feedstocks: From Mechanistic Electrocatalysis Models to System Design. *Adv. Mater.* **31**, 1807166 (2019).

7 Song, J. T. *et al.* Nanoporous Au Thin Films on Si Photoelectrodes for Selective and Efficient Photoelectrochemical CO_2 Reduction. *Adv. Energy Mater.* **7**, 1601103 (2017).

8 Gu, J., Héroguel, F., Luterbacher, J. & Hu, X. Densely Packed, Ultra Small SnO Nanoparticles for Enhanced Activity and Selectivity in Electrochemical CO_2 Reduction. *Angew. Chem., Int. Ed.* **57**, 2943-2947 (2018).

9 Kumar, B. *et al.* Reduced SnO_2 Porous Nanowires with a High Density of Grain Boundaries as Catalysts for Efficient Electrochemical CO_2-into-HCOOH Conversion. *Angew. Chem., Int. Ed.* **56**, 3645-3649 (2017).

10 Fan, L., Xia, Z., Xu, M., Lu, Y. & Li, Z. 1D SnO_2 with Wire-in-Tube Architectures for Highly Selective Electrochemical Reduction of CO_2 to C1 Products. *Adv. Funct. Mater.* **28**, 1706289 (2018).

11 Liu, G. *et al.* Black reduced porous SnO_2 nanosheets for CO2 electroreduction with high formate selectivity and low overpotential. *Appl. Catal. B: Environ.* **260**, 118134 (2020).

12 Li, F., Chen, L., Knowles, G. P., MacFarlane, D. R. & Zhang, J. Hierarchical Mesoporous SnO2 Nanosheets on Carbon Cloth: A Robust and Flexible Electrocatalyst for CO2 Reduction with High Efficiency and Selectivity. *Angew. Chem., Int. Ed.* **56**, 505-509 (2017).

13 Baruch, M. F., Pander, J. E., III, White, J. L. & Bocarsly, A. B. Mechanistic Insights into the Reduction of CO_2 on Tin Electrodes using in Situ ATR-IR Spectroscopy. *ACS Catal.* **5**, 3148-3156 (2015).

14 Zhang, W., Chang, J. & Yang, Y. Strong precious metal–metal oxide interaction for oxygen reduction reaction: A strategy for efficient catalyst design. *SusMat* **3**, 2-20 (2023).

15 Salvini, C., Re Fiorentin, M., Risplendi, F., Raffone, F. & Cicero, G. Active Surface Structure of SnO_2 Catalysts for CO_2 Reduction Revealed by Ab Initio Simulations. *J. Phys. Chem. C* . **126**, 14441-14447 (2022).

16 Lee, S. H. *et al.* Oxidation State and Surface Reconstruction of Cu under CO_2 Reduction Conditions from In Situ X-ray Characterization. *J. Am. Chem. Soc.* **143**, 588-592 (2021).

17 Lai, W. *et al.* Dynamic Evolution of Active Sites in Electrocatalytic CO_2 Reduction Reaction: Fundamental Understanding and Recent Progress. *Adv. Funct. Mater.* **32**, 2111193 (2022).

18 Ross, M. B. *et al.* Designing materials for electrochemical carbon dioxide rcycling. *Nat. Catal.* **2**, 648-658 (2019).

19 Gao, D., Arán-Ais, R. M., Jeon, H. S. & Roldan Cuenya, B. Rational catalyst and electrolyte design for CO_2 electroreduction towards multicarbon products. *Nat. Catal.* **2**, 198-210 (2019).

20 Kothary, P. *et al.* Superhydrophobic hierarchical arrays fabricated by a scalable colloidal lithography approach. *J. Colloid Interface Sci.* **487**, 484-492 (2017).

21 Niu, Z.Z. *et al.* Hierarchical Copper with Inherent Hydrophobicity Mitigates Electrode Flooding for High-Rate CO_2 Electroreduction to Multicarbon Products. *J. Am. Chem. Soc.* **143**, 8011-8021 (2021).

22 Ma, M., Djanashvili, K. & Smith, W. A. Controllable Hydrocarbon Formation from the Electrochemical Reduction of CO2 over Cu Nanowire Arrays. *Angew. Chem., Int. Ed.* **55**, 6680-6684 (2016).

23 Yang, B. *et al.* Accelerating CO_2 Electroreduction to Multicarbon Products via Synergistic Electric–Thermal Field on Copper Nanoneedles. *J. Am. Chem. Soc.* **144**, 3039-3049 (2022).

24 Liu, M. *et al.* Enhanced electrocatalytic CO_2 reduction via field-induced reagent concentration. *Nature* **537**, 382-386 (2016).

25 Atrak, N., Tayyebi, E. & Skúlason, E. Insight into Catalytic Active Sites on TiO_2/RuO_2 and SnO_2/RuO_2 Alloys for Electrochemical CO_2 Reduction to CO and Formic Acid. *ACS Catal.*, 5491-5501 (2023).

26 Salvini, C., Re Fiorentin, M., Risplendi, F., Raffone, F. & Cicero, G. Active Surface Structure of SnO_2 Catalysts for CO_2 Reduction Revealed by Ab Initio Simulations. *J. Phys. Chem. C* **126**, 14441-14447 (2022).

27 Hsu, P.C. *et al.* Sputtering Deposition of P-Type SnO Films with SnO_2 Target in Hydrogen-Containing Atmosphere. *ACS Appl. Mater. Interfaces* **6**, 13724-13729 (2014).

28 Meng, L. *et al.* Highly selective triethylamine sensing based on SnO/SnO_2 nanocomposite synthesized by one-step solvothermal process and sintering. *Sens. Actuators B Chem.* **342**, 130018 (2021).

29 Du, W. *et al.* Role of oxygen migration on the thermal stability of the perpendicular magnetic anisotropy in bottom and top structures. *APL Mater.* **10**, 011101 (2022).

30 Ren, Z. *et al.* Thermal Assisted Oxygen Annealing for High Efficiency Planar CH3NH3PbI3 Perovskite Solar Cells. *Sci. Rep.* **4**, 6752 (2014).

31 Diéguez, A. *et al.* Morphological analysis of nanocrystalline SnO_2 for gas sensor applications. *Sens. Actuators B Chem.* **31**, 1-8 (1996).

32 Vijayarangamuthu, K. & Rath, S. Nanoparticle size, oxidation state, and sensing response of tin oxide nanopowders using Raman spectroscopy. *J. Alloys Compd.* **610**, 706-712 (2014).

33 Diéguez, A., Romano-Rodríguez, A., Vilà, A. & Morante, J. R. The complete Raman spectrum of nanometric SnO_2 particles. *J. Appl. Phys.* **90**, 1550-1557 (2001).

34 Shen, X. *et al.* Dual-Site Cascade Oxygen Reduction Mechanism on SnOx/Pt–Cu–Ni for Promoting Reaction Kinetics. *J. Am. Chem. Soc.* **141**, 9463-9467 (2019).

35 Yamamoto, S. *et al.* In situ x-ray photoelectron spectroscopy studies of water on metals and oxides at ambient conditions. *J. Condens. Matter Phys.* **20**, 184025 (2008).

36 Lee, B. *et al.* Modification of Electronic Properties of Graphene with Self-Assembled Monolayers. *Nano Lett.* **10**, 2427-2432 (2010).

37 Flynn, M. R. & Bush, J. W. M. Underwater breathing: the mechanics of plastron respiration. *J. Fluid Mech.* **608**, 275 - 296 (2008).

38 Trogadas, P. & Coppens, M.O. Nature-inspired electrocatalysts and devices for energy conversion. *Chem. Soc. Rev* **49**, 3107-3141 (2020).

39 Iwata, R. *et al.* Bubble growth and departure modes on wettable/non-wettable porous foams in alkaline water splitting. *Joule* **5**, 887-900 (2021).

40 Khan, S., Hwang, J., Horn, Y.S. & Varanasi, K. K. Catalyst-proximal plastrons enhance activity and selectivity of carbon dioxide electroreduction. *Cell Rep. Phys. Sci.* **2**, 100318 (2021).

41 Xing, Z., Hu, L., Ripatti, D. S., Hu, X. & Feng, X. Enhancing carbon dioxide gas-diffusion electrolysis by creating a hydrophobic catalyst microenvironment. *Nat. Commun.* **12**, 136 (2021).

42 Shi, R. *et al.* Efficient wettability-controlled electroreduction of CO_2 to CO at Au/C interfaces. *Nat. Commun.* **11**, 3028 (2020).

43 Angulo, A., van der Linde, P., Gardeniers, H., Modestino, M. & Fernández Rivas, D. Influence of Bubbles on the Energy Conversion Efficiency of Electrochemical Reactors. *Joule* **4**, 555-579 (2020).

44 Panchanathan, D., Rajappan, A., Varanasi, K. K. & McKinley, G. H. Plastron Regeneration on Submerged Superhydrophobic Surfaces Using In Situ Gas Generation by Chemical Reaction. *ACS Appl. Mater. Interfaces* **10**, 33684-33692 (2018).

45 Verho, T. *et al.* Reversible switching between superhydrophobic states on a hierarchically structured surface. *Proc. Natl. Acad. Sci.* **109**, 10210-10213 (2012).

46 Li, J. *et al.* Efficient electrocatalytic CO_2 reduction on a three-phase interface. *Nat. Catal.* **1**, 592-600 (2018).

47 De Luna, P. *et al.* Catalyst electro-redeposition controls morphology and oxidation state for selective carbon dioxide reduction. *Nat. Catal.* **1**, 103-110 (2018).

48 Zhang, W. *et al.* Surface oxygenation induced strong interaction between Pd catalyst and functional support for zinc–air batteries. *Energy Environ. Sci.* **15**, 1573-1584 (2022).

49 Handoko, A. D., Wei, F., Jenndy, Yeo, B. S. & Seh, Z. W. Understanding heterogeneous electrocatalytic carbon dioxide reduction through operando techniques. *Nat. Catal.* **1**, 922-934 (2018).

50 Dutta, A., Kuzume, A., Rahaman, M., Vesztergom, S. & Broekmann, P. Monitoring the Chemical State of Catalysts for CO_2 Electroreduction: An In Operando Study. *ACS Catal.* **5**, 7498-7502 (2015).

51 Wang, P. *et al.* Phase and structure engineering of copper tin heterostructures for efficient electrochemical carbon dioxide reduction. *Nat. Commun.* **9**, 4933 (2018).

52 Casebolt, R., Levine, K., Suntivich, J. & Hanrath, T. Pulse check: Potential opportunities in pulsed electrochemical CO_2 reduction. *Joule* **5**, 1987-2026 (2021).

53 Timoshenko, J. *et al.* Steering the structure and selectivity of CO_2 electroreduction catalysts by potential pulses. *Nat. Catal.* **5**, 259-267 (2022).

54 Kim, C., Weng, L.C. & Bell, A. T. Impact of Pulsed Electrochemical Reduction of CO_2 on the Formation of C^{2+} Products over Cu. *ACS Catal.* **10**, 12403-12413 (2020).

55 Diéguez, A., Romano-Rodríguez, A., Vilà, A. & Morante, J. R. The complete Raman spectrum of nanometric SnO_2 particles. *J. Appl. Phys.* **90**, 1550-1557 (2001).

56 Wuttig, A., Yaguchi, M., Motobayashi, K., Osawa, M. & Surendranath, Y. Inhibited proton transfer enhances Au-catalyzed CO_2-to-fuels selectivity. *Proc. Natl. Acad. Sci.* **113**, E4585-E4593 (2016).

57 Chernyshova, I. V., Somasundaran, P. & Ponnurangam, S. On the origin of the elusive first intermediate of CO_2 electroreduction. *Proc. Natl. Acad. Sci.* **115**, E9261-E9270 (2018).

58 Fried, S. D. & Boxer, S. G. Measuring Electric Fields and Noncovalent Interactions Using the Vibrational Stark Effect. *Acc. Chem. Res.* **48**, 998-1006 (2015).

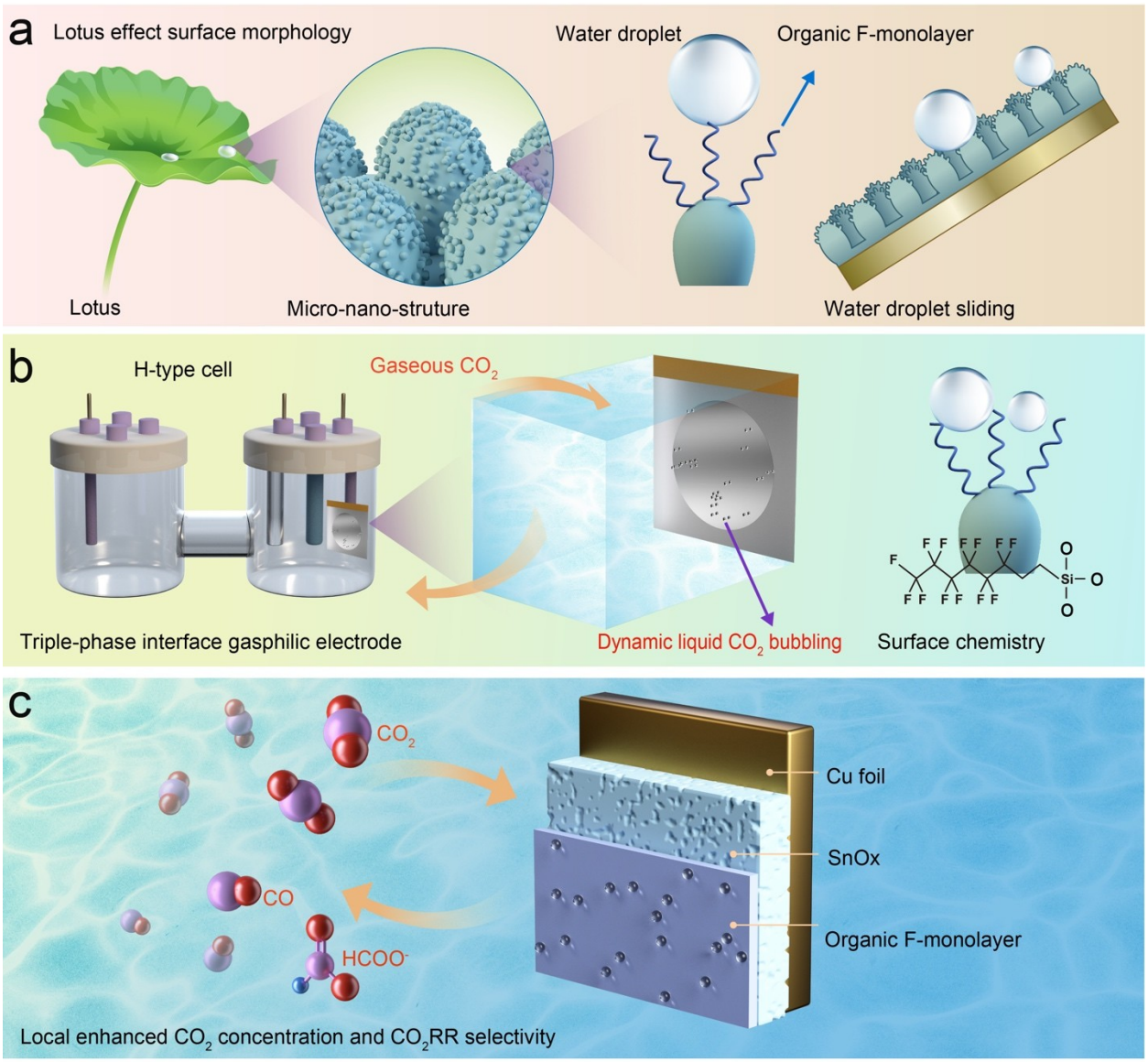

Figure 1. Schematics of the "lotus" structured gasphilic SnO_x porous film for CO_2 proactive capture and reduction. (a). Schematuc illustration of "lotus" micro-nano structure on SnO_x porous film coated with organic F-monolayer and its superhydrophobic behavior; (b). Schematuc illustration of efficient dynamic liquid CO_2 bubbling enhanced CO_2RR process in aqueous electrolyte on triple-phase gasphilic interface; (c). Schematuc configuration of BGPF electrode during CO_2RR in aqueous electrolyte and reaction pathway.

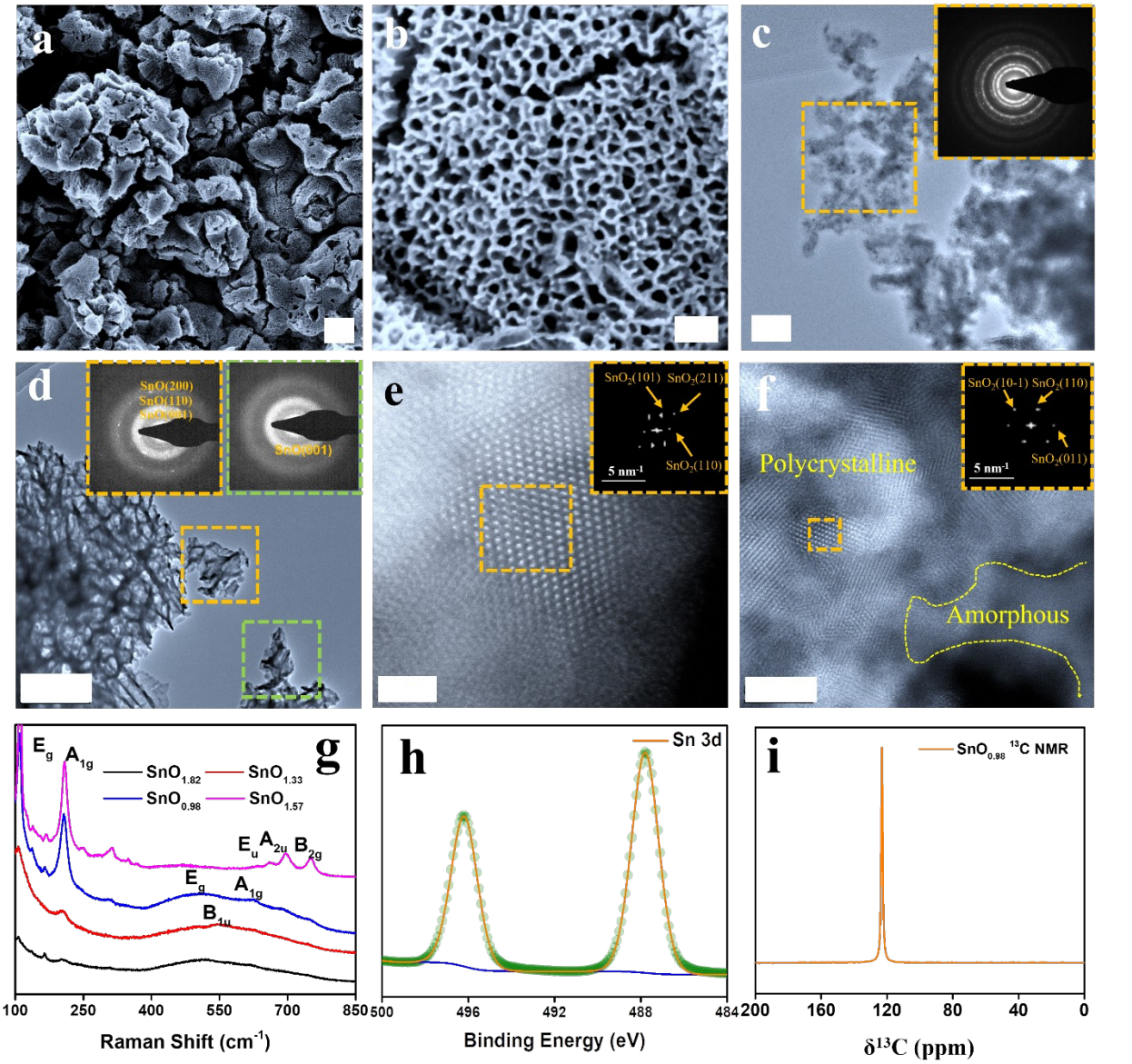

Figure 2. Structural characterizations of thermal-driven phase modulation of hierarchically porous SnO_x films. (a) Top-view SEM image of the porous structure. (b) Enlarged SEM image of the porous structure. HAADF-STEM images of (c) $SnO_{1.82}$, (d) $SnO_{1.33}$, (e) $SnO_{0.98}$, (f) $SnO_{1.57}$. (g) Raman spectra of $SnO_{1.82}$, $SnO_{1.33}$, $SnO_{0.98}$, and $SnO_{1.57}$. (h) XPS Sn 3d spectrum of $SnO_{0.98}$. (i) Direct excitation ^{13}C MAS (magic angle-spinning) NMR spectra of CO_2-adsorbed $SnO_{0.98}$ porous film. Scale bars: (a) 1 μm, (b-c) 100 nm, (d) 200 nm, (e) 2 nm, and (f) 5 nm.

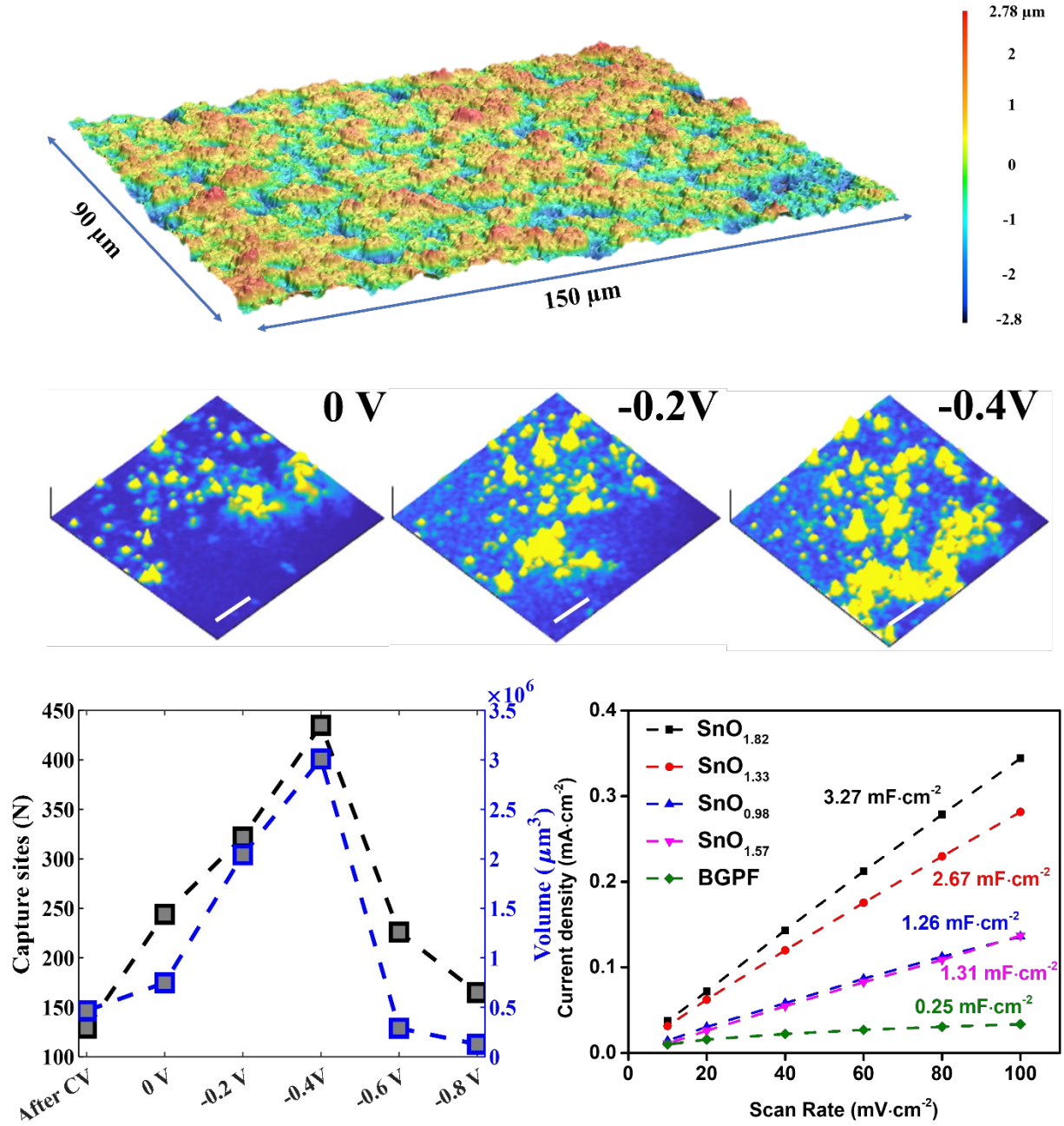

Figure 3. "Plastron"-like interface of hierarchically porous BGPF electrode. (a) Confocal scanning laser microscopy image demonstrating surface morphology. (b) Surface morphological images of the BGPF electrode during CO_2 bubbling under constant potentials at 0 V, -0.2 V, and -0.4 V during CO_2RR (scale bar: 40 µm). (c) CO_2-capturing properties of the BGPF electrode in CO_2-saturated 0.5 M $KHCO_3$ electrolyte: quantification of potential-dependent CO_2-capturing sites and volume variance. (d) Calculated capacitance plotted against CV scan rates for different samples, derived from non-faradaic current.

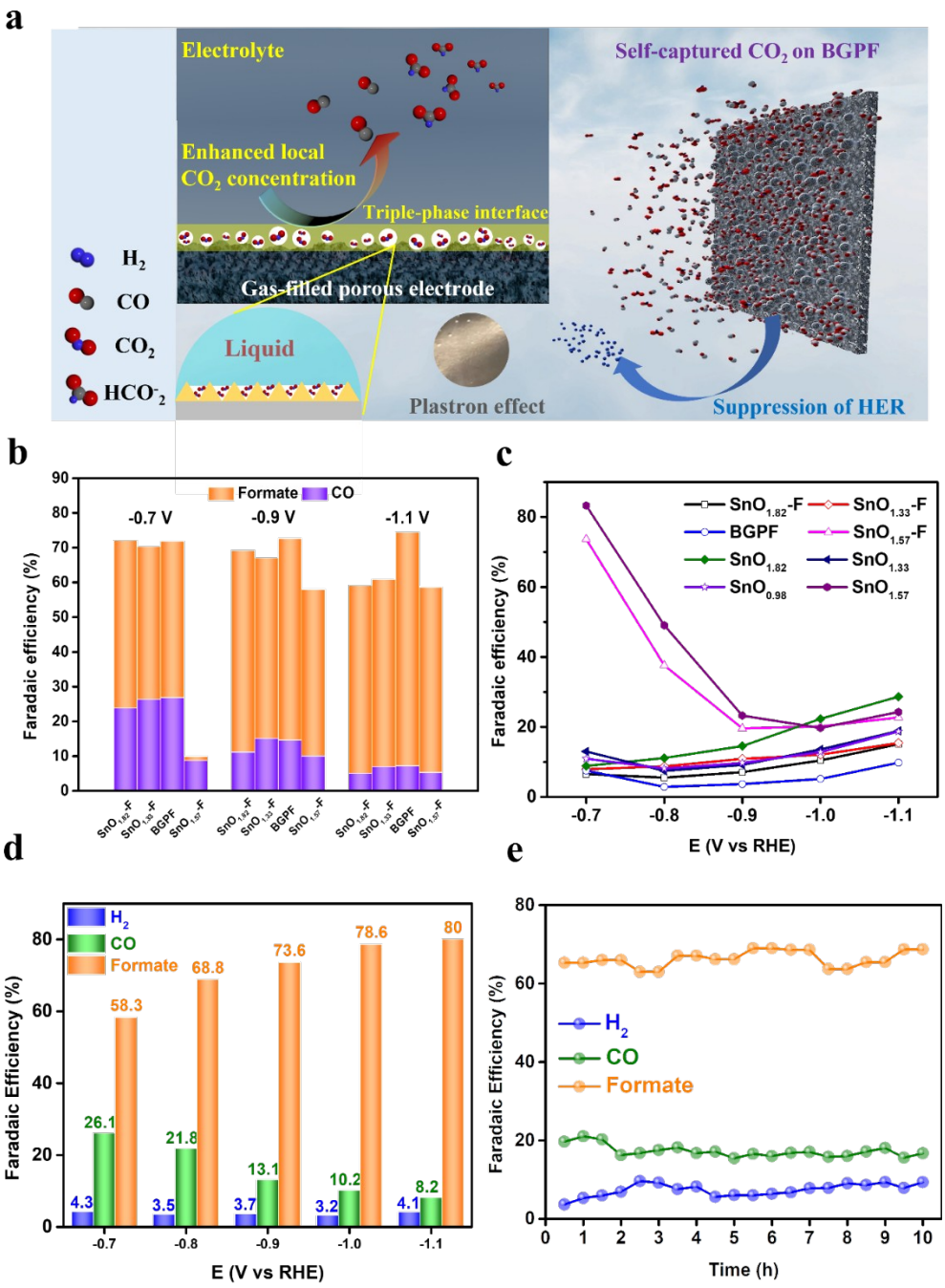

Figure 4. Electrochemical performance of hierarchically porous SnO_x films. (a) Schematic illustration providing a mechanistic understanding of efficient CO_2RR on the gas-capturing BGPF electrode. (b) CO_2RR faradaic efficiency of BGPF, $SnO_{1.82}$-F, $SnO_{1.33}$-F, and $SnO_{1.57}$-F electrodes under different constant potentials. (c) Comparison of HER faradaic efficiency of the porous films under different constant potentials during CO_2RR. (d) CO_2RR faradaic efficiency of the BGPF electrode in pulsed conditions at different potentials (Δt_c = 60s and Δt_a = 5s, applied cyclically). (e) CO_2RR faradaic efficiency of the BGPF electrode under pulsed electrochemical conditions (Δt_c = 60s at -0.8 V and Δt_a = 5s at 0.2 V, applied cyclically) during a 10 h stability test.

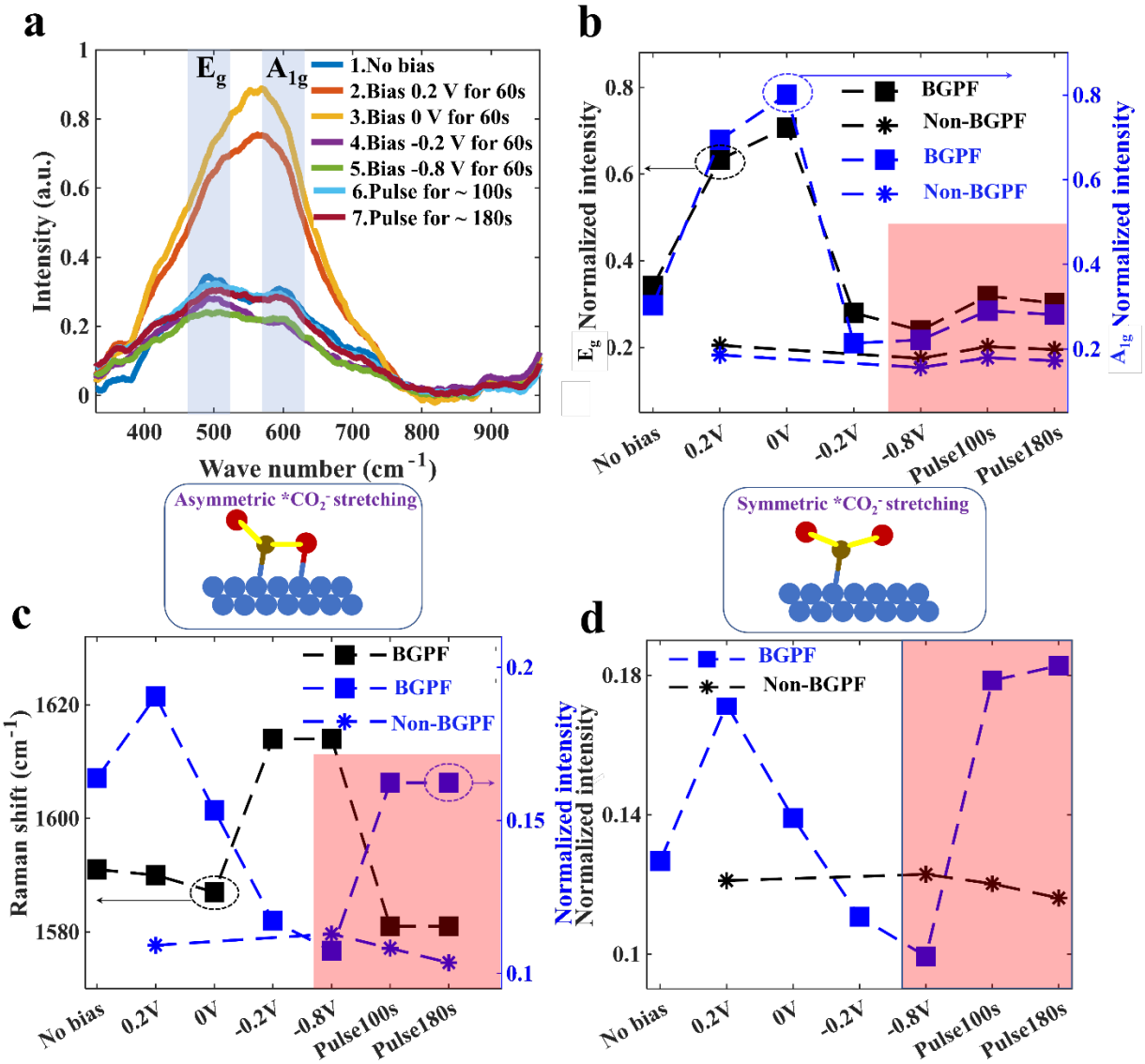

Figure 5. Mechanistic study of dynamic recovery of surface active phase. (a) *In-situ* Raman spectroscopy of BGPF under different electrochemical conditions. (b) Influence of electrochemical potentials on the intensity of E_g and A_{1g} vibrational modes centered around 476 cm^{-1} and 623 cm^{-1}, respectively. (c, d) Effect of electrochemical potentials on the intensity and Raman shift of the carboxylate $*CO_2^-$ intermediate, determined from the *in-situ* Raman spectra of BGPF at the specific Raman shift ranges of 1580-1620 cm^{-1} and 1335 cm^{-1}, respectively. The shaded areas indicate the regions where the CO_2RR process was observed.

Table of Contents

The bio-inspired strategy of proactive CO_2 capture and reduction at the modified triple-phase interface of rationally designed porous SnO_x film allows for selective and stable CO_2 conversion to value-added fuels, incorporating principles of interface engineering and pulsed electrochemistry.